Instantaneous Pressure Determination from Unsteady Velocity Fields Using Adjoint-based Sequential Data Assimilation

Chuangxin HE（何创新）[1, 2], Yingzheng LIU（刘应征）[1, 2]* & Lian GAN（干联）[3]

[1] *Key Lab of Education Ministry for Power Machinery and Engineering*
School of Mechanical Engineering, Shanghai Jiao Tong University
800 Dongchuan Road, Shanghai 200240, China

[2] *Gas Turbine Research Institute, Shanghai Jiao Tong University*
800 Dongchuan Road, Shanghai 200240, China

[3] *Department of Engineering, Durham University*
Durham DH1 3LE, UK

Manuscript revised in February 2020

* Corresponding author:
E-mail address: yzliu@sjtu.edu.cn (Y.Z. Liu)

Abstract

A sequential data assimilation (DA) method is developed for pressure determination of turbulent velocity fields measured by particle image velocimetry (PIV), based on the unsteady adjoint formulation. A forcing term $\boldsymbol{F}$, which is optimised using the adjoint system, is added to the primary Navier-Stokes (N-S) equations to drive the assimilated flow toward the observations at each time step. Compared with the conventional unsteady adjoint method, which requires the forward integration of the primary system and the backward integration of the adjoint system, the present approach integrates the primary-adjoint system all the way forward, discarding the requirement of data storage at every time step, being less computationally resource-consuming, and saving space. The pressure determination method of integration from eight paths (Dabiri et al., 2014) is also evaluated for comparison. Using synthetic PIV data of a turbulent jet as the observational data, the present DA method is able to determine the instantaneous pressure field precisely, using the three-dimensional velocity fields, regardless of the observational noise. For the two-dimensional three-component (3C) or two-component (2C) velocity fields, which are not sufficient for pressure determination by the integration method due to the lack of off-plane derivatives, the present DA method is able to reproduce pressure fields whose statistics agree reasonably well with those of the referential results. The 3C and 2C velocity fields yield quite similar results, indicating the possibility of pressure determination from only planar-PIV measurements in turbulent flows. The tomography PIV (tomo-PIV) measurements are also used as observational data and a clear pressure pattern is obtained with the present DA method.

Keywords: data assimilation, pressure determination, adjoint formulation, tomo-PIV

1. Introduction

Pressure fluctuations in turbulent flow fields are closely associated with flow-induced vibrations and sound emissions[1]. Although pressure signals can be acquired using pointwise measurement devices such as pressure transducers and microphones, the determination of two- or three-dimensional pressure fields inside the flow field is critically important for the analysis of turbulence-acoustic coupling mechanisms[2] and flow control strategies for noise reduction[3]. Currently there are not reliable and efficient measurement techniques to directly acquire instantaneous pressure fields within turbulent flow fields. The development of time-resolved tomography particle image velocimetry (tomo-PIV) enables acquisition of three-dimensional velocity fields in turbulent flows[4, 5], and pressure fields can be indirectly obtained from tomo-PIV data by spatial integration of the pressure gradients or by solving the Poisson equation[6, 7]. This strategy has numerous successful applications in various flow conditions[8-10]. However, due to the high noise level of tomo-PIV measurements, and the requirements on domain size, resolution and sampling rate for pressure determination, this method has limitations in complex flow situations[11, 12]. Therefore, the development of a reliable alternative method for the accurate and efficient determination of unsteady pressure fields is highly desirable.

Pressure determination from velocity fields enables a nonintrusive measurement, at high spatial resolution, of the pressure field that matches the state of art of PIV measurements. In the integration method, given a time-resolved velocity field typically measured by PIV, the pressure gradient field can be recovered by coupling the velocity data with Navier-Stokes (N-S) equations[6],

$$\nabla p = -\rho \frac{D\boldsymbol{U}}{Dt} + \mu \nabla^2 \boldsymbol{U} = -\rho \frac{\partial \boldsymbol{U}}{\partial t} - \rho(\boldsymbol{U} \cdot \nabla)\boldsymbol{U} + \mu \nabla^2 \boldsymbol{U} \quad (1)$$

where $D\boldsymbol{U}/Dt$ is the material acceleration treated from either Lagrangian or Eulerian perspectives, ρ is the fluid density, and μ denotes the dynamic viscosity. The pressure can thus be determined by spatially integrating the pressure gradient from a reference point in a specified path. Alternatively, the pressure field can also be obtained by solving the Poisson equation

$$\nabla^2 p = -\rho \nabla \cdot (\boldsymbol{U} \cdot \nabla)\boldsymbol{U} \quad (2)$$

under the assumption that the flow field is divergence free. Although these two approaches are equivalent in theory, their implementation and computational procedures have significant effects on their resultant pressure distributions, due to their different properties of error propagation and accumulation[13]. These differences have considerable influence on pressure determination. Liu and Katz[14] proposed a virtual boundary omni-directional integration algorithm for pressure determination to minimise the effect of local random errors. This approach requires large computational efforts, which are prohibitive in large-scale three-dimensional computations. Alternatively, selecting only eight integration paths[15] substantially reduces the computational cost, and has good accuracy in pressure determination for certain flow configurations. Although the integration and Poisson approaches are successful at instantaneous pressure field determination from PIV measurements[16-19], several difficulties that prevent their wide application are rarely considered. First, due to the three-dimensional nature of turbulent flows, instantaneous pressure fields cannot be accurately recovered from planar- or stereo-PIV measurements[6, 20]. Eqns. (1) and (2) demonstrate that off-plane derivatives give non-negligible contributions to the pressure gradient or Laplacian, and thus fully three-dimensional measurement techniques are required such as tomo-PIV[7, 21]. Second, a high sampling rate of the PIV measurement is needed for the determination of the time-derivative term. Indeed, the error of the time-derivative term increases with a decrease in sampling rate. Meanwhile, the time-derivative, and thus the pressure fluctuation, are usually over-predicted due to PIV noise along the time direction[11]. Third, these approaches are subject to effects of the boundary condition, especially when only a small region of flow field is obtained, which is common in tomo-PIV measurements, or when the instantaneous pressure on the boundaries cannot be considered constant. These issues limit the application of the integration method to flows with large-scale organised patterns and much higher pressure variations than those resulting from computational error. These limitations must be properly addressed before this method can be widely used.

Rather than calculating the pressure field based on Eqns. (1) and (2) from existing velocity

data such as PIV measurements, data assimilation (DA) can be used to recover the global velocity field from existing local data, and the pressure field can be determined simultaneously using the standard velocity-pressure coupling algorithm in computational fluid dynamics (CFD). DA is a mathematical technique that was initially developed for numerical weather prediction[22]. It gathers observational (experimental) data at a given time and uses equations from flow dynamics and thermodynamics to estimate the future atmospheric state. It can also be used for the uncertainty quantification and improvement of the turbulence closures[23-25]. The adjoint-based DA technique has received increasing attention for flow predictions within which the adjoint equation system, including the corresponding boundary conditions, are derived and solved together with the primary equation system[26, 27]. The time-averaged flow and pressure fields can thus be accurately predicted within constraints from local measurement data. Lemke and Sesterhenn[28] could compute instantaneous pressure fields from synthetic velocity data (without noise) using an unsteady continuous adjoint formulation. When applied to real PIV data, lower recovery accuracy was observed, due to the two-dimensional assimilation of the three-dimensional flow[29]. For an unsteady adjoint system, the integration should be performed forward for the primary equations and backward for the adjoint equations. Therefore, data must be saved for all time steps[30], resulting in large storage space requirements and slow processing speeds.

As a follow-up study of the mean-flow DA techniques based on the continuous adjoint formulation[26], this study proposes a sequential DA scheme for instantaneous turbulent flow and pressure fields. The adjoint system is designed without the requirement of the backward integration, and thus data can be saved at large time intervals. The formulation is implemented in the open-source code OpenFOAM (http://openfoam.org). Synthetic data of a circular turbulent jet[31], which simulates the planar-, stereo- and tomo-PIV measurements, are used as observations. We then compare the resultant instantaneous velocity and pressure fields, and their statistical properties. Finally, three-dimensional data from tomo-PIV measurements are used to test the pressure determination capacity of the method.

2. Mathematic Formulation

The present adjoint-based DA formulation is derived from the time-dependent Navier-Stokes (N-S) equations, where a forcing term $\boldsymbol{F}$ is added and is optimised to minimise the discrepancy between the observational data and the predictions.

$$\frac{\partial \boldsymbol{U}}{\partial t} + (\boldsymbol{U} \cdot \nabla)\boldsymbol{U} = \frac{1}{\rho}\nabla p - \nu \nabla^2 \boldsymbol{U} + \boldsymbol{F} \tag{3}$$

$$\nabla \cdot \boldsymbol{U} = 0 \tag{4}$$

Here, ν denotes the kinematic viscosity of the fluid. For turbulent flows, this formulation approaches an implicit large-eddy simulation (LES), where the contribution of the subgrid vortical structures has been partially absorbed in $\boldsymbol{F}$. Importantly, this strategy is different from that used in the steady-state DA formulation[26], where the S-A model is used and a correcting coefficient is determined. The underlying reason is that the use of the eddy-viscosity model enables a robust computation of the primary and adjoint equation systems in steady-state cases, while a forcing term added directly to the N-S equation facilitates a quick response of the flow to the optimisation procedure in unsteady cases. Indeed, the turbulence model can also be used without modification, by replacing ν with $\nu + \nu_t$ in Eqn. (3), where ν_t denotes the turbulent or subgrid eddy viscosity.

The present DA technique can be achieved by minimising the cost function $\mathcal{J}$ subject to the governing equations, using an optimised distribution of $\boldsymbol{F}$. This is expressed as

$$\text{minimise } \mathcal{J} = \xi \int_{t_0}^{T} \int_{\Omega} M \left(\frac{\boldsymbol{U} - \boldsymbol{U}_{\text{Exp}}}{U_\infty} \right)^2 \mathrm{d}\Omega \mathrm{d}t, \text{ subject to } \mathcal{R}(\boldsymbol{U}, p, \boldsymbol{F}) = 0. \tag{5}$$

Here t_0 and T are the initial and terminal times between which DA is performed. Ω represents the computational domain. A masking function M is defined to specify the region where the observational data are obtained. ξ is a dimension converter of dimensions $[\mathrm{L}^2 \cdot \mathrm{T}^{-3}]$ and value unity to cope with the dimensional inconsistency. $\mathcal{R} = (\mathcal{R}_{\mathrm{NS}}, \mathcal{R}_{\mathrm{C}})$ denotes the incompressible unsteady N-S equations and the continuity equation. We thus obtain a constraint optimisation problem solvable by introducing a Lagrange function $\mathcal{L}$ such that

$$\mathcal{L} = \mathcal{J} + \int_{t_0}^{T} \int_{\Omega} (\boldsymbol{V}, q) \mathcal{R} \mathrm{d}\Omega \mathrm{d}t, \tag{6}$$

Here, the adjoint velocity $\boldsymbol{V}$ and the adjoint pressure q are introduced as the Lagrange multipliers. The determination of the optimal $\boldsymbol{F}$ distribution can be achieved by obtaining the sensitivities of the Lagrange function $\mathcal{L}$ with respect to the state variables. The total variation of $\mathcal{L}$ can be calculated as

$$\delta\mathcal{L} = \delta_{\boldsymbol{U}}\mathcal{L} + \delta_p\mathcal{L} + \delta_{\boldsymbol{F}}\mathcal{L} \tag{7}$$

This can be simplified by choosing the appropriate adjoint variables $\boldsymbol{V}$ and q to deplete the variation with respect to the state variables,

$$\delta_{\boldsymbol{U}}\mathcal{L} + \delta_p\mathcal{L} = 0 \tag{8}$$

The sensitivities can be obtained using the variation in $\mathcal{L}$ with respect to $\boldsymbol{F}$.

$$\delta\mathcal{L} = \delta_{\boldsymbol{F}}\mathcal{J} + \int_{t_0}^{T} \int_{\Omega} (\boldsymbol{V}, q)\, \delta_{\boldsymbol{F}}\mathcal{R} \mathrm{d}\Omega \mathrm{d}t \tag{9}$$

According to Eqn. (8), the adjoint equations associated with the adjoint state variables $\boldsymbol{V}$ and q can be derived as

$$\delta_{\boldsymbol{U}}\mathcal{J} + \delta_p\mathcal{J} + \int_{t_0}^{T} \int_{\Omega} (\boldsymbol{V}, q)\, \delta_{\boldsymbol{U}}\mathcal{R} \mathrm{d}\Omega \mathrm{d}t + \int_{t_0}^{T} \int_{\Omega} (\boldsymbol{V}, q)\, \delta_p\mathcal{R} \mathrm{d}\Omega \mathrm{d}t = 0 \tag{10}$$

with

$$\delta_{\boldsymbol{U}}\mathcal{R}_{\mathrm{NS}} = \frac{\partial \delta\boldsymbol{U}}{\partial t} + (\delta\boldsymbol{U} \cdot \nabla)\boldsymbol{U} + (\boldsymbol{U} \cdot \nabla)\delta\boldsymbol{U} - \nu\nabla^2\delta\boldsymbol{U} \tag{11}$$

$$\delta_{\boldsymbol{U}}\mathcal{R}_{\mathrm{C}} = -\nabla \cdot \delta\boldsymbol{U} \tag{12}$$

$$\delta_p\mathcal{R}_{\mathrm{NS}} = \frac{1}{\rho}\nabla\delta p \tag{13}$$

$$\delta_p\mathcal{R}_{\mathrm{C}} = 0 \tag{14}$$

Therefore, the adjoint equations and the corresponding boundary conditions are shown below.

Adjoint equations:

$$\frac{\partial \boldsymbol{V}}{\partial t} + (\boldsymbol{V} \cdot \nabla)\boldsymbol{U} - (\boldsymbol{U} \cdot \nabla)\boldsymbol{V} - \nu\nabla^2\boldsymbol{V} + \frac{1}{\rho}\nabla q + 2\xi M \frac{\boldsymbol{U} - \boldsymbol{U}_{\mathrm{Exp}}}{U_\infty^2} = 0 \tag{15}$$

$$\nabla \cdot \boldsymbol{V} = 0 \tag{16}$$

Adjoint boundary conditions:

For the inflow, the wall and far-field boundaries where the primary state variable $\boldsymbol{U}$ is specified, the boundary conditions are

$$\boldsymbol{V}_\tau = 0, \qquad \boldsymbol{V}_n = 0 \tag{17}$$

$$\boldsymbol{n} \cdot \nabla q = 0 \tag{18}$$

For the outflow boundaries where the zero-gradient condition is used for the primary state variables $\boldsymbol{U}$, the conditions are

$$U_n \cdot V_\tau + \nu(\boldsymbol{n} \cdot \nabla) U_\tau = 0 \tag{19}$$

$$U_n \cdot V_n + \nu(\boldsymbol{n} \cdot \nabla) U_n - q = 0 \tag{20}$$

Here, the subscripts n and τ denote the normal and tangential components of the variables, respectively. $\boldsymbol{n}$ is the unit normal vector at the boundaries.

Terminal condition:

When $t_0 = T$ in Eqn. (10), the terminal condition at $t = T$ can be derived as

$$\boldsymbol{V}(T) = 0 \tag{21}$$

As noted previously[26], Eqn. (19) provides a tangential component condition that is highly sensitive to the primary velocity, which induces serious instability for the adjoint equations. Fortunately, this outflow boundary condition contributes little to the adjoint flow field inside the domain. The zero-gradient condition for the adjoint velocity on the outflow boundary is a good choice to significantly improve the numerical stability without deterioration of the results. The second numerical stability issue noted previously[26] was from the adjoint transpose convection (ATC) term, and thus the first-order upwind scheme was applied for the convection term of the adjoint momentum equations. However, this stability issue does not occur in the solution of the present unsteady equations, and thus all of the equations retain second-order accuracy.

Once the adjoint state variables are obtained, the sensitivities of the Lagrange function $\mathcal{L}$ with respect to the forcing $\boldsymbol{F}$ can be computed from Eqn. (9) as

$$\frac{\partial \mathcal{L}}{\partial \boldsymbol{F}} = -\boldsymbol{V} \tag{22}$$

As the sensitivity with respect to the state variables is forced to vanish (Eqn. (8)), the forcing $\boldsymbol{F}$ can be adjusted gradually according to Eqn. (22) to minimise the cost function. This is achieved using the steepest descent algorithm[32] at each iteration (the iteration procedure is shown in Figure 1). $\boldsymbol{F}$ can then be determined as

$$\boldsymbol{F} = \boldsymbol{F} - \lambda \frac{\partial \mathcal{L}}{\partial \boldsymbol{F}} \tag{23}$$

where λ is the step length, estimated as

$$\lambda = \alpha / \left(\frac{\partial \mathcal{L}}{\partial \boldsymbol{F}} \right)_{\max} \tag{24}$$

Here $\alpha = (0.01 \sim 0.1)[L^{-1}]$. It is important to note that Eqn. (24) is only a rough estimation of λ according to the results of the first several time steps. A larger λ leads to rapid convergence of the computation, but is less robust, while a smaller λ results in a more robust convergence in computation but requires more iteration steps to reduce the residual (defined in Eqn. (25)) to the same level.

$$\varepsilon_U = \int_\Omega \frac{|\boldsymbol{U} - \boldsymbol{U}_{Exp}|}{|\boldsymbol{U}_{Exp}|} d\Omega \tag{25}$$

However, the selection of λ is not critical in this study. A slightly smaller λ value can be used to enhance the numerical stability, as the residual keeps decreasing with time even with a fixed iteration number. For PIV measurements with high noise levels, smaller residuals yield an assimilated flow closer to the measurements, indicating that high noise levels are contained in the results as well. In this situation, using a smaller λ to slightly increase the residual is workable to reduce the noise in the assimilated global flows.

Conventional unsteady adjoint methods require forward integration for the primary equations, but backward integration for the adjoint system in the duration $[t_0, T]$. This necessitates the use of

a small time interval, and saving the data at all time steps, as each iteration is conducted with a forward and a backward loop. To reduce the time and space requirements for the storage and reading-writing processes, the time duration in which the adjoint optimisation is performed is reduced from $[t_0, T]$ to $[t_0, t_1]$ where t_1 $(t_1 \ll T)$ denotes the next adjacent time step with respect to t_0. This suggests that the adjoint optimisation process is performed for each time step individually, rather than for a large duration with all of the data. Therefore, Eqn. (15) can be modified using the Euler difference scheme for the time derivative,

$$\left(\frac{\boldsymbol{V}-\boldsymbol{V}_{\mathrm{Ter}}}{\Delta t}\right)+(\boldsymbol{V}\cdot\nabla)\boldsymbol{U}-(\boldsymbol{U}\cdot\nabla)\boldsymbol{V}-\nu\nabla^2\boldsymbol{V}+\frac{1}{\rho}\nabla q+2\xi M\frac{\boldsymbol{U}-\boldsymbol{U}_{\mathrm{Exp}}}{U_\infty^2}=0 \tag{26}$$

Here $\boldsymbol{V}_{\mathrm{Ter}}=0$ is the terminal condition of the adjoint velocity according to (21. The adjoint N-S equation thus becomes

$$\frac{\boldsymbol{V}}{\Delta t}+(\boldsymbol{V}\cdot\nabla)\boldsymbol{U}-(\boldsymbol{U}\cdot\nabla)\boldsymbol{V}-\nu\nabla^2\boldsymbol{V}+\frac{1}{\rho}\nabla q+2\xi M\frac{\boldsymbol{U}-\boldsymbol{U}_{\mathrm{Exp}}}{U_\infty^2}=0 \tag{27}$$

This produces steady adjoint equations that are solvable with the unsteady primary equations at each iterative loop.

It is noted that (27 is derived using the Euler scheme which is first-order accurate in time. However, this has no much deterioration on the final results since the temporal discretization of primary equations still remains second-order accurate. The error induced by this Euler scheme finally enters the residual plateau ((25) which only denotes the gap between the predictions and the observations but not the credibility of the results themselves. Thus the time step in the computation can be determined according to the Courant Number $\mathrm{Co} \approx 1-2$. The spatial discretization keeps second-order accurate for both primary and adjoint equations. According to the synthetic jet case in section 3.2 where the results are written every 20 time steps, 95% storage space and the reading/writing time can be saved compared to the conventional unsteady adjoint formulation.

The iteration procedure is demonstrated in Figure 1. The primary equations Eqns. (3) and (4) are solved using an initial condition with the forcing term $\boldsymbol{F}=0$. If the observational data are

present, the convergence (whether the residual ε_U is lower than a specified value ε) is evaluated once the primary equations are solved. Otherwise, the computation skips the adjoint system and directly starts the next time step of the primary equations, which is identical to conventional CFD procedures. If the convergence criterion is reached, or the iteration number n is larger than a specified value N for a time step when the observational data are present, the computation jumps to the next time step and starts a new time loop. Otherwise, the steady adjoint equations Eqns. (27) and (16) are solved and the forcing term $\boldsymbol{F}$ is updated according to Eqn. (23). Thus, the primary equations are solved again, and the computation starts a new iterative loop. The total computational cost of this DA process is less than 10% higher than conventional CFD simulations using the same grid in the present study.

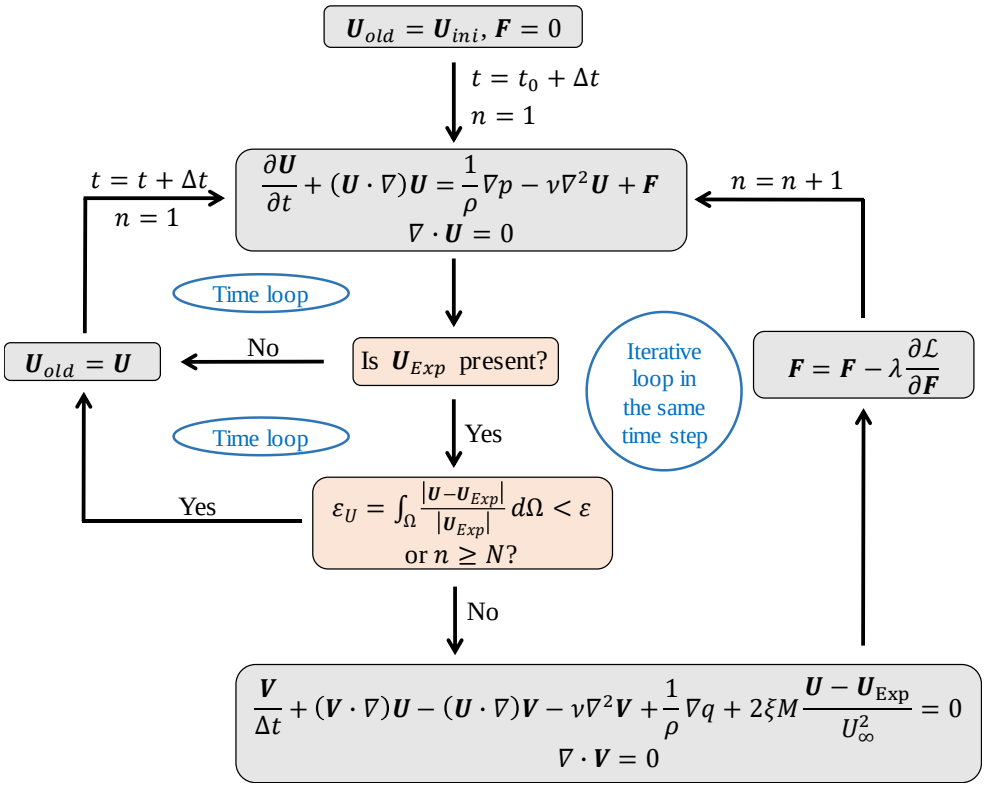

Figure 1 Iteration procedure of the primary-adjoint system. n is the iterative loop number and t denotes the physical time.

3. Results and Discussion

3.1 Two-dimensional cylinder wake

A two-dimensional cylinder wake is used to demonstrate the basic performance of the present DA method and to compare the pressure field reconstruction ability of the method with the conventional integration approach. The computational domain has a width of $20D$ where D is the diameter of the cylinder. The inflow boundary is located $5D$ upstream of the cylinder and the outflow boundary extends to $30D$ downstream. A structured grid is used with the element number 160 distributed azimuthally on the cylinder. The Reynolds number of the flow is fixed at $Re = 100$ so that the flow is two-dimensional. The direct numerical simulation (DNS) is performed with the maximum Courant number approximately 1, and the results at each time step are stored. The flow (both components of the velocity) is selected in a rectangular window with width $3D$ at $0.75 \leq x/D \leq 4.75$, to be representative of a PIV field of view, and is used as the referential observational data ("Ref"). In the DA computation, the primary velocity is initialised using the instantaneous field, which exhibits different phases compared with the corresponding observational data. A quite small targeted residual is set, and the maximum iteration loop number is fixed at 20. This forces the primary-adjoint system to be iterated for 20 loops before switching to the next time step when the observational data are present.

Figure 2 shows the instantaneous streamwise velocity fields of the reference DNS (Ref), and those obtained by the DA method at different time steps using a λ value of 10^{-4} (the selection of λ will be discussed below in reference to Figure 3). The black solid box in the left column represents the region where the observational data are involved in DA. There is no constraint outside of the solid box and thus the flow develops freely. It can be determined from Figure 2 (a) and (b) by comparing the flow in the solid and dashed boxes that a significantly different phase of the wake is used as the initial condition in the first steps. Despite this, rapid convergence enables

the flow in the observational window to develop almost identically with the flow in the reference field as shown in Figure 2 (c) and (d). The adjoint system drives the assimilated flow to be closer to the reference data specifically in the observational window, as the flow outside of the window remains significantly different. The flow downstream of the window in Figure 2 (c) still maintains the historical information inherited from the initial field, while long-term development of the flow enables the assimilated information to be advected downstream, causing the flow downstream of the window to approach that of the referential field as shown in Figure 2 (e) and (f). This is an important property of the present DA method, where the observational data and the prediction model (the N-S equation in this case) combine to produce better results than can be obtained by the individual usage of either method alone.

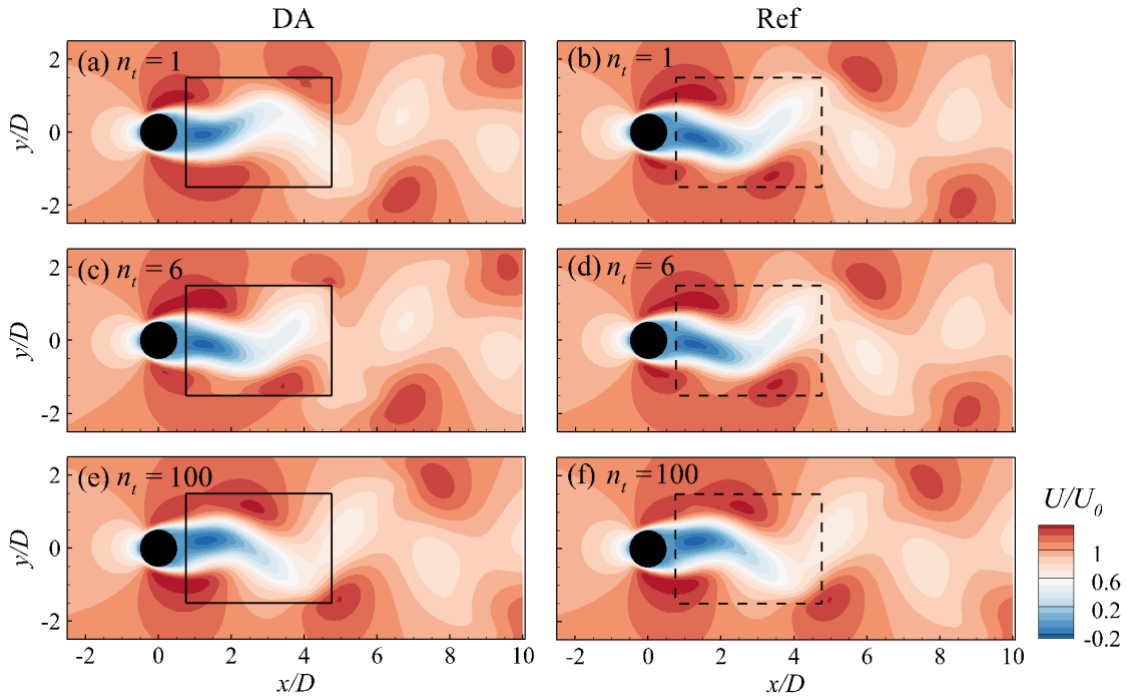

Figure 2 Instantaneous streamwise velocity at different time steps. $\lambda = 10^{-4}$, n_t denotes the time step number, left column: DA, right column: Reference. Referential data in the dashed box is used as the observation in DA

The downstream extension of the assimilated information can be clearly seen in Figure 3Figure 4, where time series are shown with the streamwise velocity on the centreline at $x/D = 3$ (inside the observational window) and $x/D = 6$ (outside the observational window). For $\lambda = 10^{-4}$, rapid convergence of the DA process is observed at the time step $n_t = 6$ and the location

$x/D = 3$. The discrepancy between the DA result and the reference field at $x/D = 6$ remains significant for $tU_0/D < 3$ due to the lack of observational data. This assimilated velocity becomes closer to the reference data at larger times, and finally overlaps due to the free convection. The λ value has effects on the convergence speed, but has little influence on the long-term results for a given range. This is also demonstrated in Figure 3, where both $\lambda = 10^{-3}$ and $\lambda = 10^{-4}$ yield rapid convergence of the DA process, but $\lambda = 10^{-5}$ leads to convergence only after a long period of adaptive iterations. This suggests that to a certain extent the non-strict selection of the λ value in a DA process is acceptable, even if the number of iteration loops is fixed.

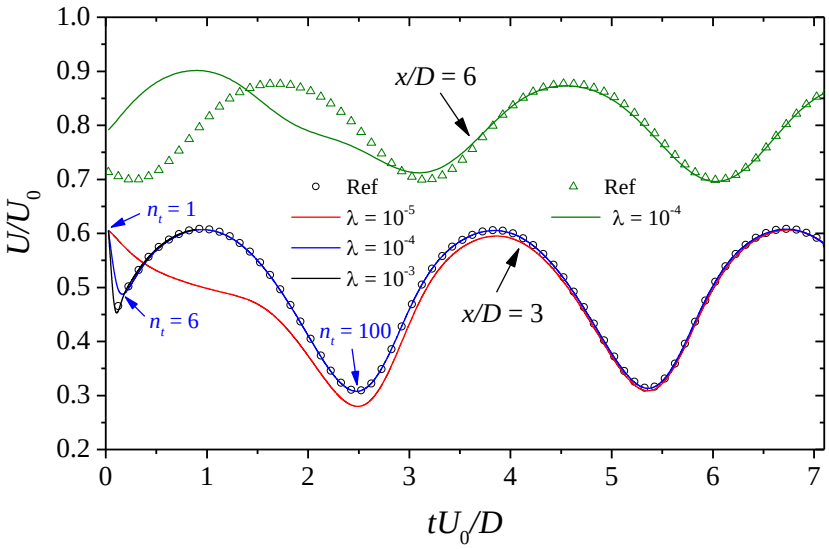

Figure 3 Time series of the streamwise velocity at $x/D = 3$ and 6 on the centreline. Different λ values are used for the evaluation of the present DA method. $n_t = 1$, 6 and 100 are marked to show the time step number.

In the assimilation process, the predicted flow is driven toward the observations by the forcing term $\boldsymbol{F}$. $\boldsymbol{F}$ decreases as the predicted flow gets closer to the observations, as can be seen in Figure 4. If the numerical model is able to recover the flow individually, $\boldsymbol{F}$ only works in the early stages (see Figure 4 (a)) due to the discrepancy between the initial conditions and the observations, and becomes significantly small at large time. If the numerical model is not accurate in predicting the flow, due to either the low grid resolution or the turbulence model defects, $\boldsymbol{F}$ prevails even at large time serving as an additional turbulence or subgrid Reynolds stress to compensate for the

discrepancy. This can be observed in the following jet flows, as the grid resolution is low and the numerical model cannot account for the disturbances and the measurement noise.

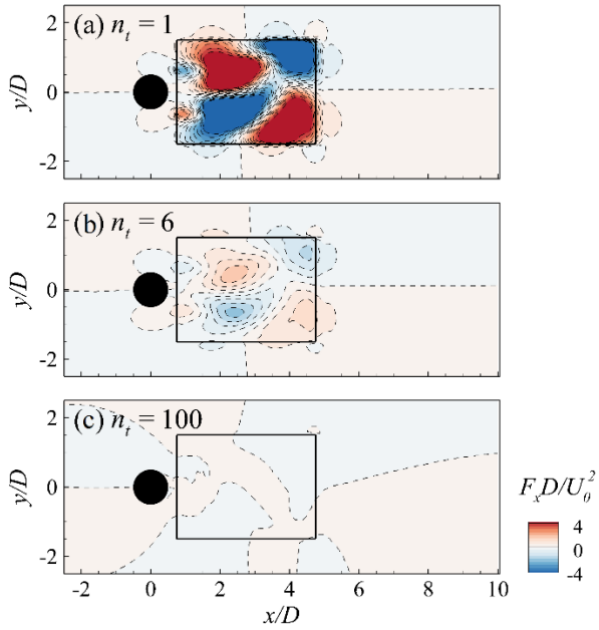

Figure 4 Streamwise component of the forcing at different time steps.

The accurate recovery of the flow field in the DA process is a prerequisite of instantaneous pressure field determination. For a two-dimensional flow, the flow field also serves as the sufficient condition once the velocity-pressure coupling process has converged when solving the primary equations. For the conventional methods of integration from the velocity gradient or solving the Poisson equation, the size of the observational window is an important parameter, and needs to be large enough to eliminate boundary effects. Figure 5 shows the pressure distributions obtained by the reference DNS, the DA technique and the integration method, respectively. Here the code developed by Dabiri et al.[15] is used for pressure field determination as shown in Figure 5(c) and (d). Pressure is obtained by integration of the gradient from eight paths including the vertical, horizontal and diagonal directions. As the velocity field is recovered in the DA process, the pressure is accurately determined as shown in Figure 5(a) and (b), even though only a small observational window (the solid box) is used. This accuracy is quantitatively demonstrated in Figure 6. The integration method also has good accuracy when the flow field in the whole domain is used, as

shown in Figure 5(a), except for a slight discrepancy (see Figure 6) due to the smoothing process after calculating the velocity gradients. However, this method can only determine the pressure distribution qualitatively using a small observational window as shown in Figure 5(d). The discrepancy of the pressure distribution along the centreline is quantitatively presented in Figure 6.

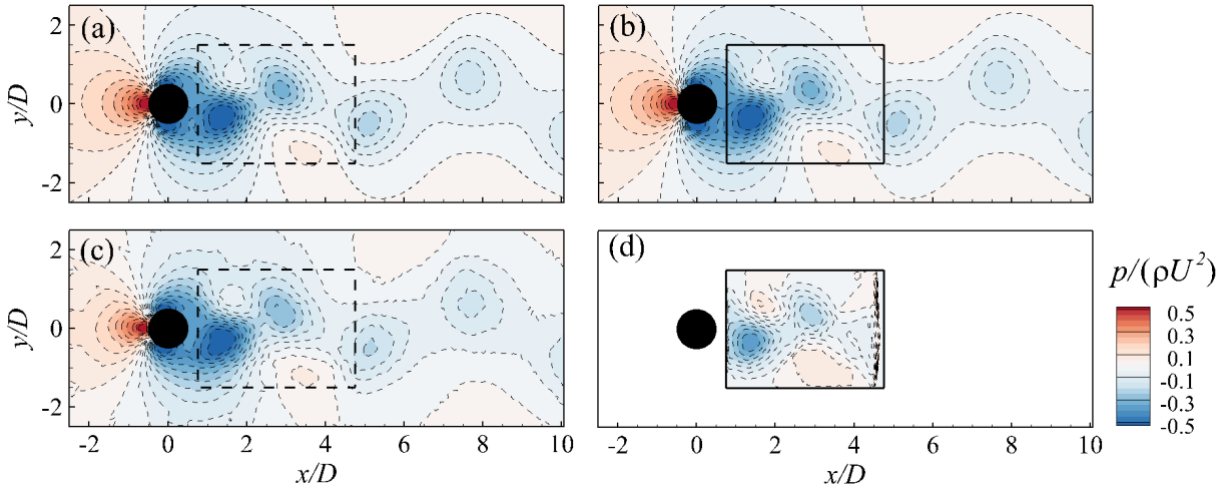

Figure 5 Pressure distributions determined by (a) referential DNS, (b) the DA process, (c) integration from pressure gradient using the whole domain and (d) integration from pressure gradient using the observational field. The solid box denotes the window in which the observational data have been used in computation, where the dashed box is shown in the same location for comparison.

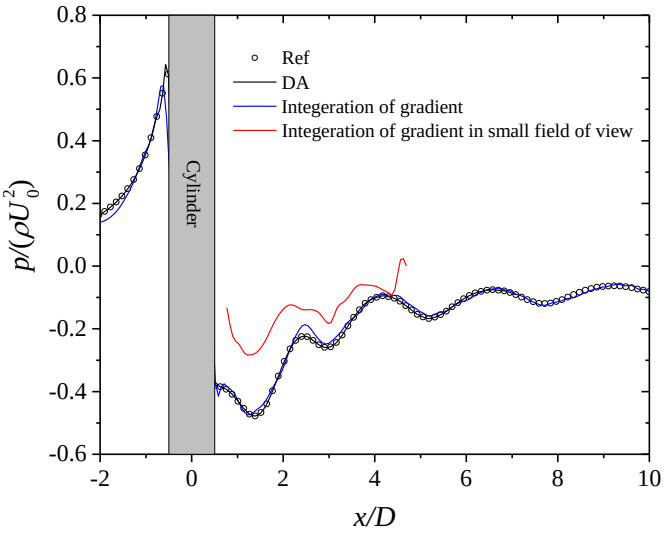

Figure 6 Pressure distributions along the centreline determined by different methods (data are extracted from Figure 5).

3.2 Three-dimensional circular jet

The three-dimensional circular jet at $Re = 6{,}000$ is employed to demonstrate the present DA properties using different observational fields. The observational data were obtained from a fine-scale LES simulation[31]. The grid, of approximately 9 million nodes, in this LES is generated by two-level refinement based on a structured O-type grid. The grid information and computational setup are described elsewhere[31]. In this DA process, the grid is obtained by one-level refinement only, with approximately 1 million nodes. A steady mean flow is imposed on the inflow boundary, rather than the fluctuating condition used in the LES simulation. Therefore, the grid resolution and the inflow conditions used in the present DA process are unable to reproduce the flow field with the same accuracy as the previous LES simulation if the observational data are not present.

The computational domain used in the present DA process is shown in Figure 7. Different observation regions are used, with ranges $0.2 \leq x/D \leq 12$ and $-2.5 \leq y/D \leq 2.5$ across different z-direction ranges. Observation I denotes the full region, in the range of $-2.5 \leq z/D \leq 2.5$, where the whole jet's cross-section is covered and which represents the large-domain tomo-PIV measurement. Observation II denotes the thin region, in the range of $-0.25 \leq z/D \leq 0.25$, representing a thin layer and which is more common in tomo-PIV measurements due to limitations in depth of field and laser intensity. Observation III denotes a two-dimensional slice on which the two-component (2C) and three-component (3C) velocity fields are considered, denoting the planar- and stereo-PIV measurements, respectively. In the present DA process, the primary velocity is initialised from the rest state. Observational data are used every 20 time steps (the time step used for the DA process is 0.005 s but the time interval of the observational data is 0.01 s). Only the primary equations are solved with $\boldsymbol{F} = 0$ if the observational data are absent.

This DA process uses a $\lambda = 1\mathrm{e}^5$ (can be estimated using (24, several orders larger than that in the cylinder case. Smaller or larger λ also works), and 20 iteration loops are used for all of the observation regions, which yields good stability and reasonable convergence for both velocity

assimilation and pressure determination. For the large observation region I, both clear LES results and those with maximum 20% white noise are used as the observational data. The observation with 20% white noise data serves as an analogue of the true PIV data with noise contamination. Figure 8 presents an instantaneous velocity field both with and without noise. Note that this field is obtained in an instance for which the observational data are present, and the residual reaches a low plateau. The velocity can be recovered accurately by this DA process, regardless of the noise contamination of the observations, even if a steady inflow condition is imposed. Moreover, this DA process has noise reduction effects, which can be seen when comparing Figure 8 (d) with (b).

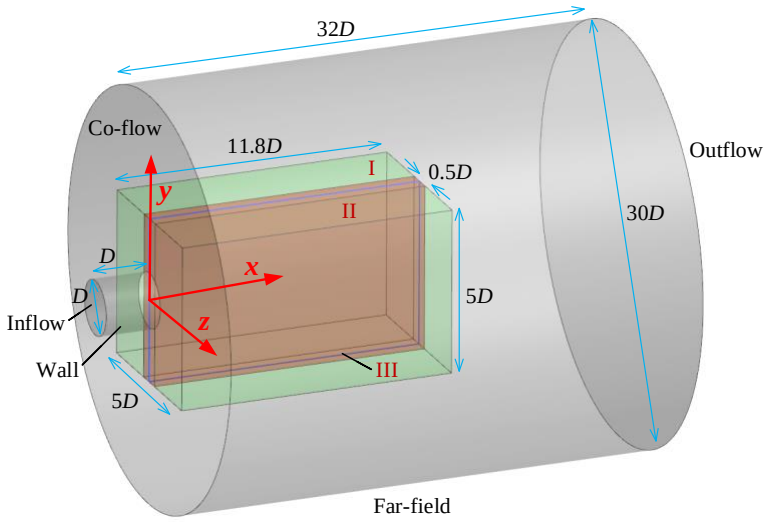

Figure 7 Computational domain and the observation region used in the present DA process.

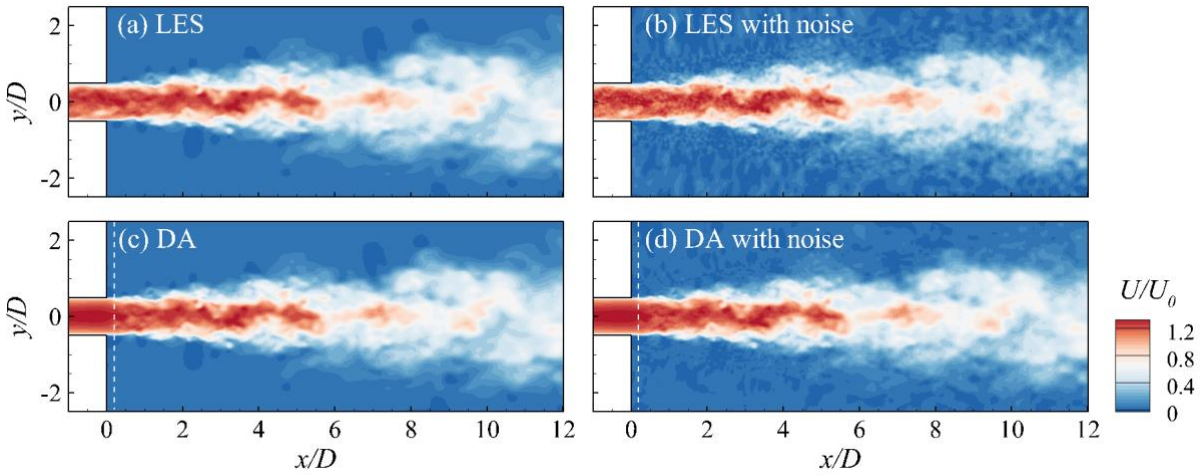

Figure 8 Instantaneous velocity fields obtained by (a-b) LES and (c-d) DA. The observation region is located downstream of the dashed line.

The DA-based pressure determination process is usually straightforward once the three-dimensional velocity is accurately recovered, as demonstrated in Figure 9, for observations both with and without noise. In this DA process, the pressure determination is based on the assimilated velocity fields rather than on the observations themselves, and thus the noise contamination from observations does not directly spread into the pressure fields, as shown in Figure 9(b) and (c) when compared with (a). This is also partially attributed to the noise reduction effects of the velocity assimilation process. It is also important to note that the pressure determination in DA is based on the zero-pressure condition at the outflow boundary, which is identical to the reference LES simulation. There will be a uniform shift of the pressure distribution if different pressure references are used, and this does not induce difficulties for applications. Moreover, as the observational data are provided once every 20 time steps, the accurate determination of the pressure fields requires that the velocity fields at the present instance and at the previous time step are also recovered precisely. When the observational data are absent, the assimilated velocity relies solely on the N-S equations. Figure 9(d) presents the pressure field determined from the integration method, using the code developed by Dabiri et al.[15] and modified by counting for the components in the z-direction. Two observational fields without noise are used for the calculation with time intervals of 0.005 s (equal to the time step in the DA process). Integration is performed through eight separate paths in the $x-y$ plane. We observe that the pressure signals display a high degree of randomness throughout the whole region, even in the ambient field. The pressure signals remain at the same level as those of both the reference LES and DA results, but the typical spatial pattern is missing. Several factors can be considered to explain this. First, the fine-scale turbulence induces high-level noise in the pressure gradient determination, even when the smoothing process is used for both pressure and its gradients, and also accumulates in the ambient field after the integration procedure. Second, the method of integration through eight paths (which is the same for omni-directional integration) requires a homogeneous condition of pressure on all the integration-starting boundaries, which is not valid in the present jet. The pressure signals for this integration method are even less accurate (data not shown) when the velocity fields have a time interval of 0.01 s, such as the observations used in the DA process.

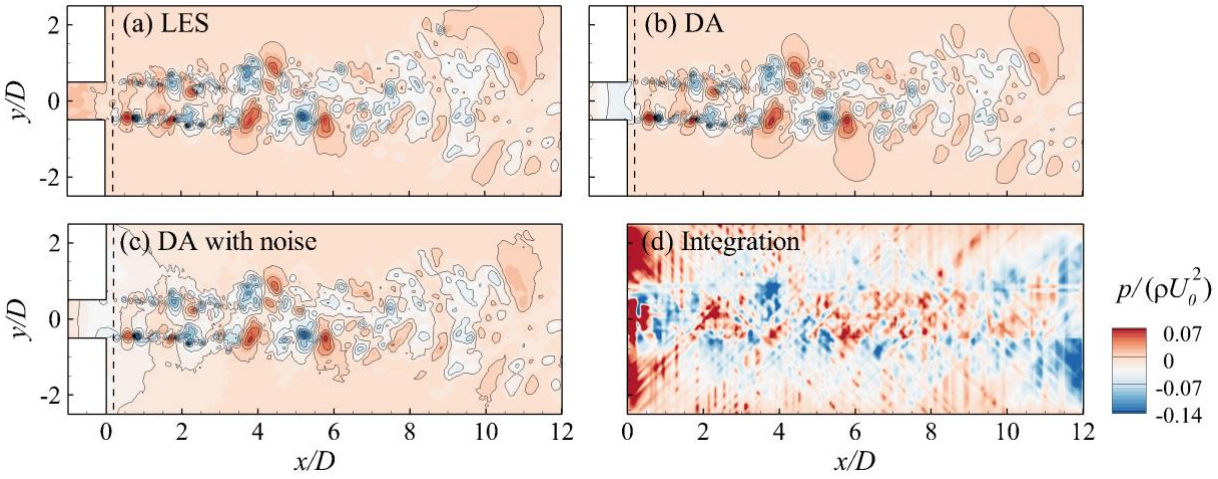

Figure 9 Instantaneous pressure fields obtained by (a) LES, (b-c) DA and (d) integration from pressure gradients without observational noise.
The observation region is located downstream of the dashed line.

Figure 10 provides a quantitative view of the velocity and pressure along the horizontal profile at $y/D = 0.5$ and $z/D = 0$. Note that for the clear observations, the assimilated velocity almost overlaps with the observational data, as demonstrated in Figure 10(a), while the slight discrepancy between the pressure distributions results from the different grid resolutions used in the reference LES and the present DA process, as shown in Figure 10(c). When higher levels of noise are involved, the assimilated velocity approaches the clear observational data, while random discrepancies can be observed between the contaminated observational data and the clear data, as shown in Figure 10(b). Indeed, the assimilated velocity can be further driven toward the noise-contaminated observational data by increasing the iteration number in each iterative loop, and thus decreasing the residual plateau. However, this requires more computational effort due to the incoherence of the flow structures in space and time, and induces noise in both velocity and pressure fields, which deteriorates the assimilation results. The selection of the iteration number is a tradeoff, considering the computational cost, the assimilation accuracy and the noise level. When 10 and 50 iterations in the iterative loop were tested, they yielded results with no major differences (results not shown). For this assimilation process, the determination of the pressure is reasonably accurate, as shown in Figure 10(d), with discrepancies in the thin shear layer due to the high shear strain. The computation of the residual defined as Eqn. (25), for the cases with and without noise

in the observational data, is plotted in Figure 11. Both computations reach the residual plateau after only 5 time steps, but the residual with the observational noise remains significantly higher than that without noise, even when using the same iteration parameters. As noted previously, further reduction of the residual plateau in the case with noise requires much more computational effort, and is thus not beneficial for noise removal in this DA process.

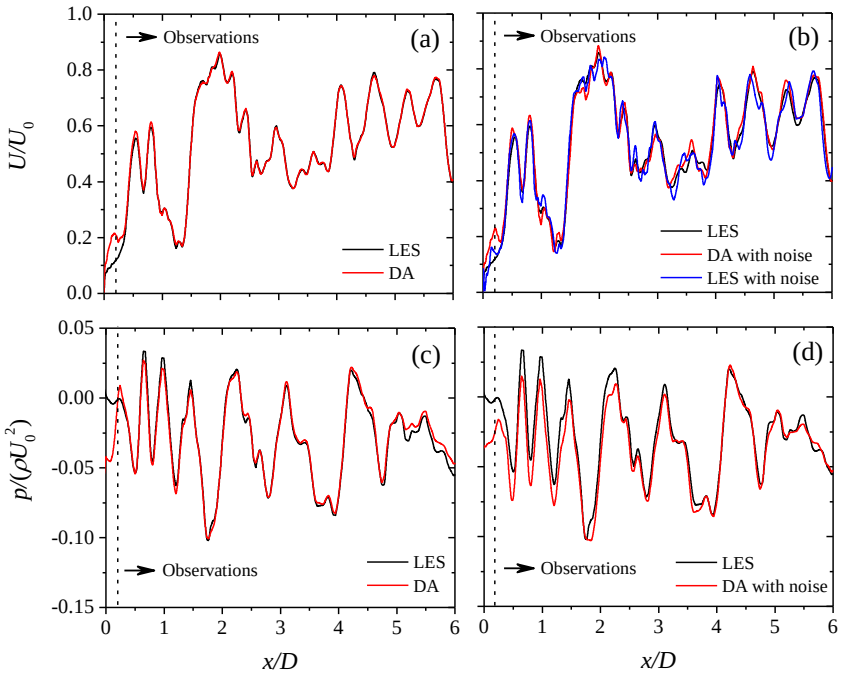

Figure 10 Instantaneous velocity distribution along the horizontal profile at $y/D = 0.5$ and $z/D = 0$. The observation region is located downstream of the dashed line.

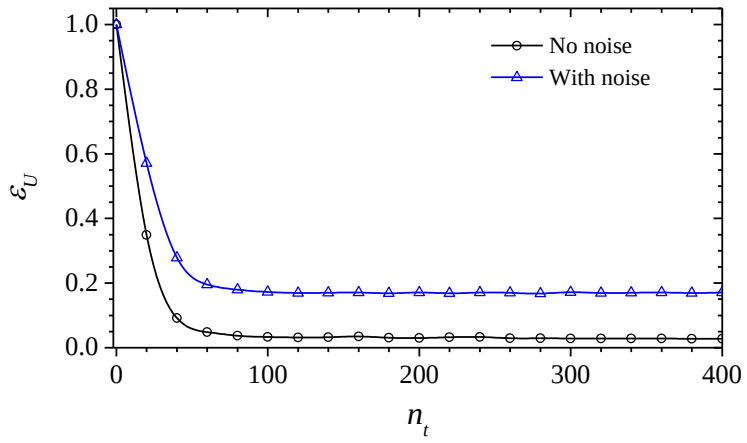

Figure 11 Computation of the residual of DA with and without observational noise.

Other important features of the present DA approach, compared with the conventional integration method, are the determination of the pressure fields using only two-dimensional velocity fields, and the improvement of the velocity and pressure predictions outside of the observation region. Here, Observation II and III (2C or 3C) are used for demonstration. These results are presented in Figure 12, together with those determined by the LES on the DA grid (i.e., coarse LES). As shown in Figure 12 (a, c, e, g, i), all of these simulations yield the precise assimilation of the flow field on the $x-y$ plane when the observational data are present. On the $x-z$ planes, there is no guarantee of recovery for the instantaneous velocity distribution, due to the lack of observational constraint. The flow develops under the limited effects of the observation region, and according to its intrinsic properties. In fact, the predictions of the flow on $x-z$ planes are improved, as shown in Figure 12(d, f, h), compared with the coarse LES shown in Figure 12(i-j). This can be discerned from the fine-scale turbulence structures developed in the jet shear layer, while only breakdown of the large-scale structures can be observed in the coarse LES.

Indeed, the pressure determination on the $x-y$ plane relies on the recovery of the three-dimensional velocities. Observation II meets this requirement, and the instantaneous pressure field can be determined very well (data not shown). This situation is quite similar to the integration method using the tomo-PIV measurements. Statistical data are plotted in Figure 13(a) and (b), and Observation II yields the mean and fluctuating pressures, which agree quite well with the reference LES. For two-dimensional observational fields, these calculations are beyond the ability of the integration method due to the lack of a velocity normal gradient. In this circular jet, the velocity gradient in the z-direction cannot be neglected due to its comparable amplitude with other components, and thus has a large contribution to the pressure field. For this DA method, however, z-direction components can be predicted with the help of the primary N-S equations. The use of the in-plane observational data yields significant improvements in determining the mean and fluctuating pressures. In contrast, the result obtained by the coarse LES exhibits significant differences from the reference LES data, especially for the pressure fluctuations in the jet shear layer. This is attributed to the failure of the large-scale vortex breakdown, and thus the induction

of excessive amplitudes in the flow and pressure fluctuations. Importantly, the 2C observations yield results with little difference from those determined using the 3C observations, which indicates that planar-PIV measurements can be used instead of stereo-PIV measurements as the observations in DA process to improve the prediction significantly.

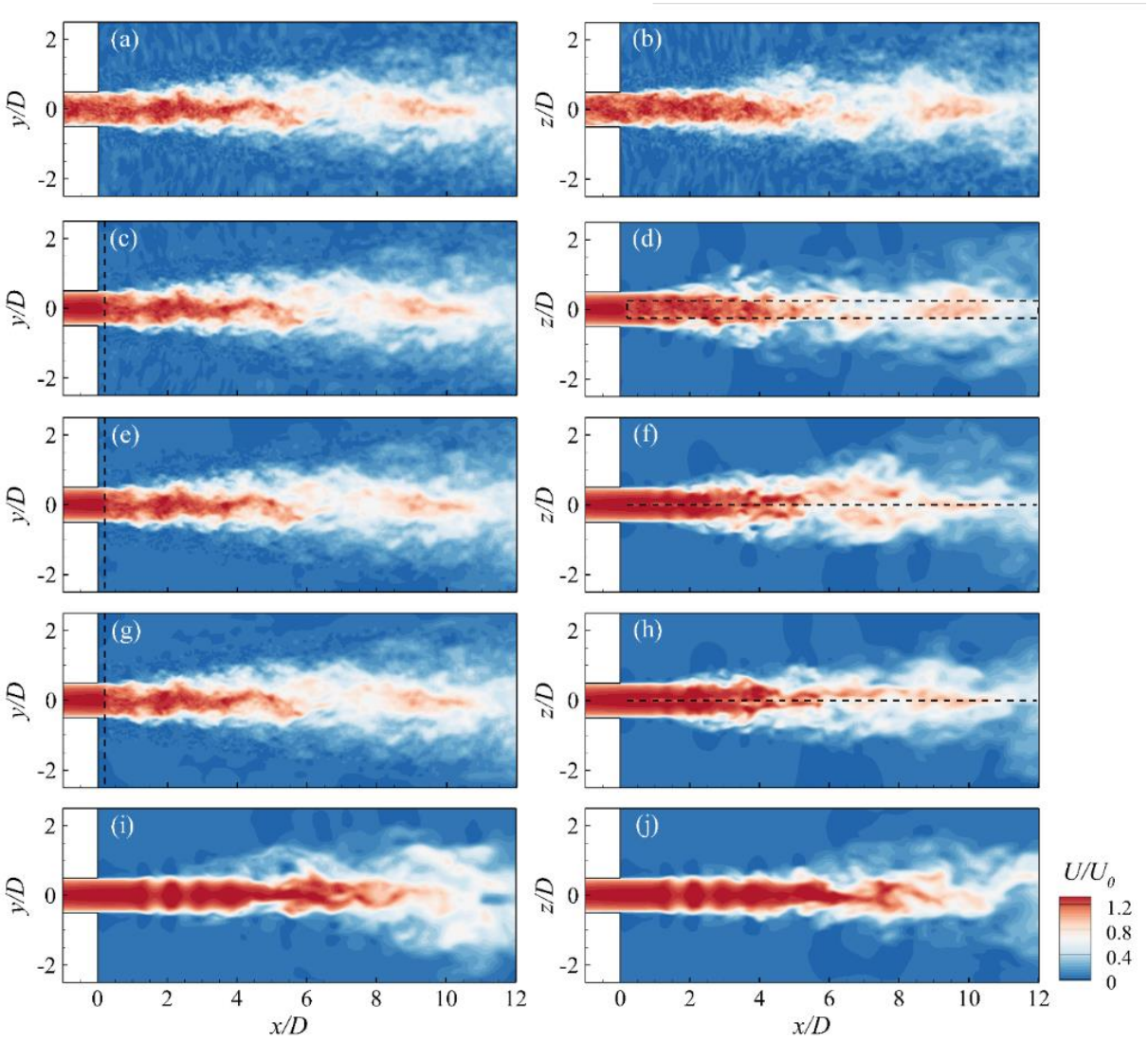

Figure 12 Comparison of the instantaneous streamwise velocity distributions on the (a, c, e, g, i) $x-y$ and (b, d, f, h, j) $x-z$ planes. (a-b) referential LES, (c-d) DA with Observation II, (e-f) DA with Observation III and 3C velocity, (g-h) DA with Observation III and 2C velocity and (i-j) coarse LES. Observation regions are indicated by the dashed lines.

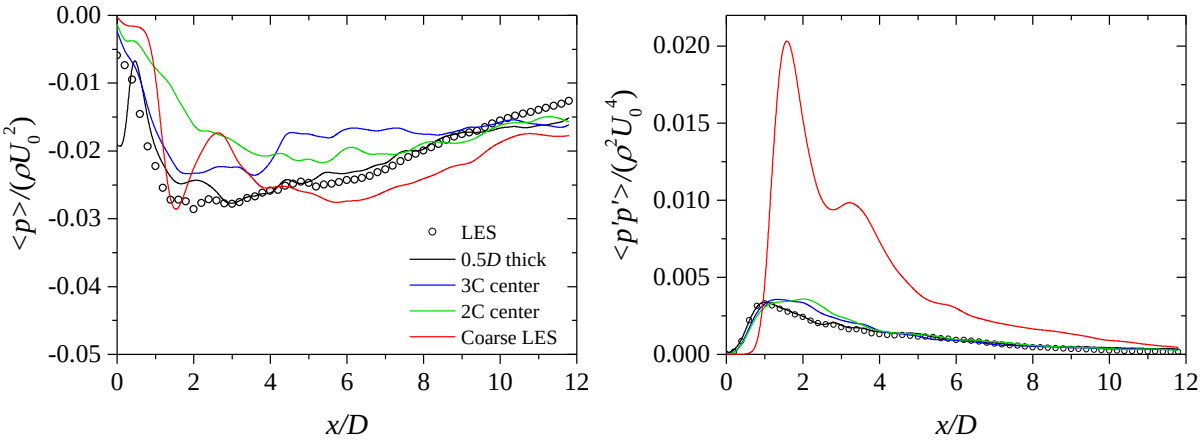

Figure 13 Comparison of the (a) mean and (b) fluctuating pressure distributions along the horizontal profiles at $y/D = 0.5$ and $z/D = 0$. Referential LES, DA with Observation II, DA with Observation III and 3C velocity, DA with Observation III and 2C velocity and coarse LES results are shown.

The prediction of the global pressure field is also inspected for the case where the observations are located in or near the $x - y$ plane. Considering the cylinder wake, in which the flow downstream of the observational window has been precisely recovered, the global fields of the jet flow are also expected to be improved, due to the spatial correlation of the assimilated flow under the influence of the local observations. Here, the azimuthal averaged mean and fluctuating streamwise velocity distributions at different downstream locations are presented in Figure 14. The fluctuations are scaled by a factor of 20 to plot the profiles in the same figure. It can be seen that the Observation II (0.5-D-thick domain) achieves reasonably good agreement with the results of the reference LES, while the two-dimensional Observation region III, with 3C and 2C velocities, yields discrepancies at $x/D = 4$ and 6. Indeed, the accuracy of the azimuthal averaged quantities strongly relies on the normal thickness of the observational domain, which can also be observed in Figure 12(d) when compared with Figure 12(f) and (h). The two-dimensional observations with 3C and 2C velocities also yield simulation results that are much better than that of the coarse LES. The azimuthal averaged mean and fluctuating pressure distributions are plotted in Figure 15. These results have similar trends to the velocity distributions. It is also noted that when using the 3C and 2C velocities on the same two-dimensional plane as the observations, the same accuracy can be

achieved for the assimilation results. This suggests that the usage of planar-PIV measurements as the observations in the present DA process, rather than stereo-PIV measurements, could simplify the measurement procedure but retain similar accuracy. Indeed, the further improvement of the assimilation results using non-full-region observations can be achieved by increasing the grid resolution. This will be considered in future work.

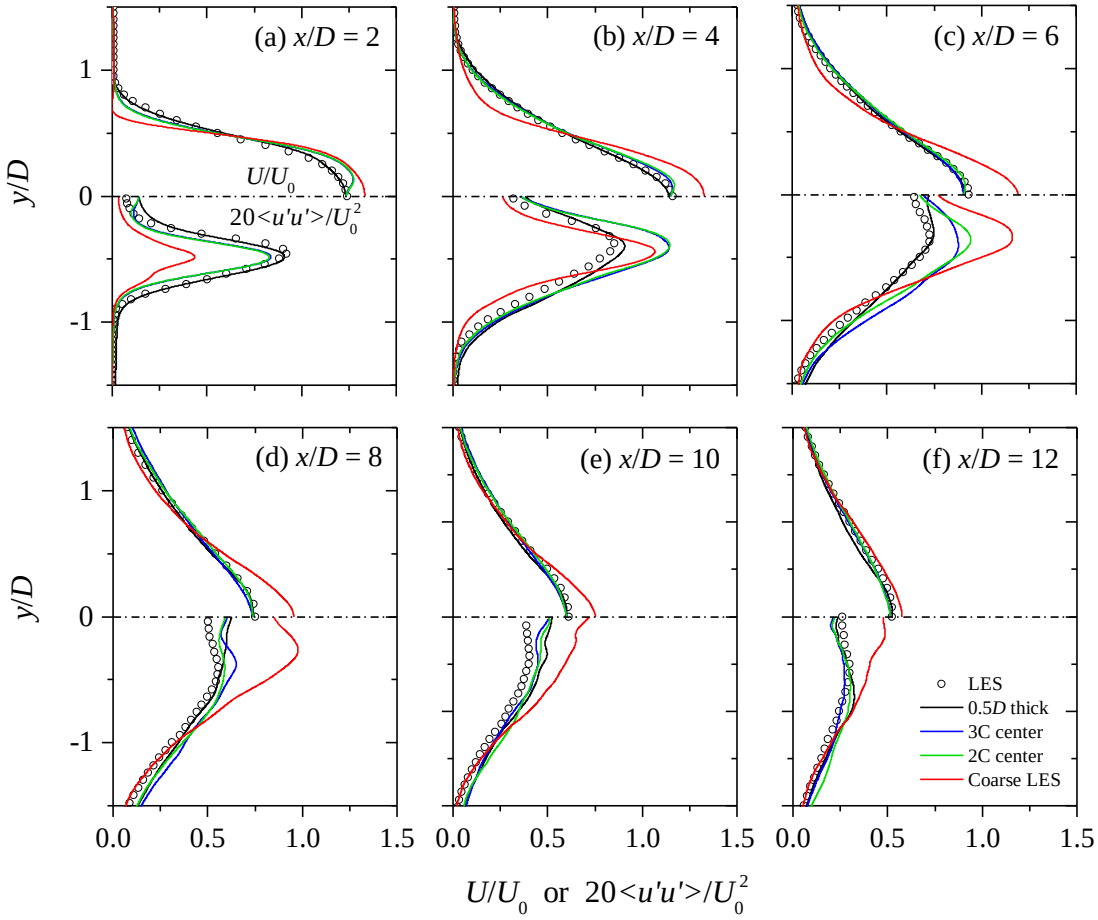

Figure 14 Azimuthal averaged mean (upper half) and fluctuating (lower half) streamwise velocity distributions. Referential LES, DA with Observation II, DA with Observation III and 3C velocity, DA with Observation III and 2C velocity and coarse LES results are shown.

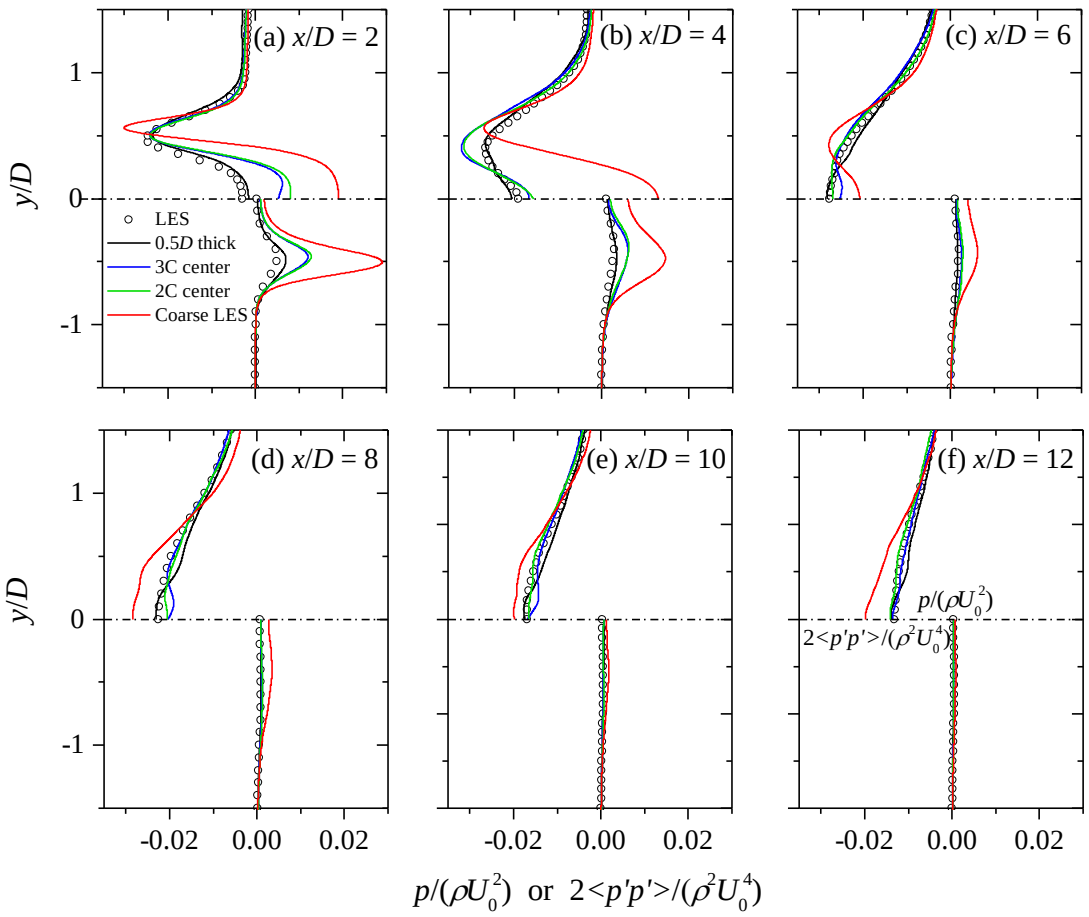

Figure 15 Azimuthal averaged mean (upper half) and fluctuating (lower half) pressure distributions. Referential LES, DA with Observation II, DA with Observation III and 3C velocity, DA with Observation III and 2C velocity and coarse LES results are shown.

3.3 Tomo-PIV measurements

The above sections discussed the properties of this DA method using numerical results as the observations, to serve as analogues for tomo-, stereo- and planar-PIV measurements. Here, real tomo-PIV measurements of a circular jet are tested as the observational data. The experiment is conducted in an octagonal tank (each side, 250 mm; height, 900 mm) filled with tap water, as shown in Figure 16. A circular nozzle with diameter $D = 40$ mm is installed at the bottom of the octagonal tank, with the exit 100 mm above the bottom surface to minimise the wall effect on the flow field. The jet fluid is supplied by a frequency-conversion pump, and first enters a stabilising chamber located below the bottom surface of the octagonal tank before nozzle ejection. The Reynolds number is based on the bulk velocity U_0 in the nozzle and the nozzle exit diameter D, and is fixed at $Re = 2400$. The global seeding of the complete tank is performed with 20-μm hollow glass particles, and illumination is realised by a 25 W continuous-wave laser at 532 nm (Millennia EV25S, USA) with a compacted combination of cylindrical lenses to produce a 25-mm-thick volumetric light on the jet longitudinal plane. Two 12-bit complementary metal-oxide-semiconductor (CMOS) cameras (PCO, Germany) with a spatial resolution of 2000 × 2000 pixels are used to capture the particle images with a frequency of 25 image pairs per second, and a time interval of 1 ms between the frames in each image pair, which yields a time interval of 0.04 s between two successive snapshots. Each camera is split into two views, as shown by the yellow dashed line in Figure 16, using an appropriate combination of prismatic and planar mirrors. This results in four different views along the radial direction, each with an image resolution of 1000 × 2000 pixels. The velocity vectors are calculated from the raw particle volumes using a TOMOpro code developed in-house[33, 34]. In the post-processing, the size of the reconstructed volume is 200 mm (x direction) × 80 mm (y direction) × 25 mm (z direction) and is centred at the nozzle axis. The multiplicative algebraic reconstruction technique (MART) is used to reconstruct the three-dimensional distributions of the particle grayscales, with a resolution of 8 voxels/mm. A sub-pixel-accurate PIV algorithm is used, based on the iterative multigrid volumetric cross-correlation approach with a final (minimum) pass, and an interrogation volume size of 24 × 24 × 24 voxels

and 50% overlap. This yields a resolution of 26 vectors per nozzle diameter D.

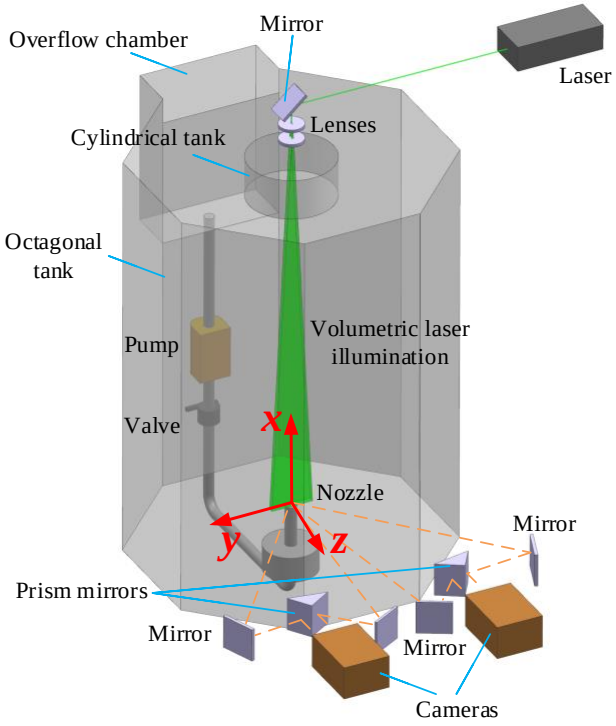

Figure 16 Experimental setup of the tomo-PIV measurement.

In this DA process, the computational domain and grid are scaled from that used with the previous reference LES (see Figure 7). The observations are set in the region $0.25 \leq x/D \leq 5$, $-1 \leq y/D \leq 1$ and $-0.5 \leq z/D \leq 0.5$ being interpolated from the tomo-PIV grid (comparable resolution with the DA grid), and are recorded every 8 time steps in DA. $\lambda = 1e^3$ (can be estimated using (24, several orders larger than that in the cylinder case. Smaller or larger λ also works), and 20 iteration loops are used for all of the observation regions, yielding reasonable convergence and acceptable noise removal for velocity assimilation and pressure determination, respectively. Figure 17 presents the instantaneous velocity fields obtained by tomo-PIV and DA methods, respectively, after the computation reaches the residual plateau. As observed, most of the field details have been recovered, including small-scale structures, after the vortex breakdown at $x/D > 3$. Due to the noise contamination in the tomo-PIV results, the converged forcing term $\boldsymbol{F}$, as shown in Figure 18, remains significantly larger compared with the case of the cylinder wake. This phenomenon was also observed in the LES jet, where the case with noise yields a higher

forcing term than that with the clear observational data. It is also observed that a larger magnitude of $\boldsymbol{F}$ is clustered in the jet shear layer, which is similar to the distributions of the turbulent eddy or subgrid viscosities.

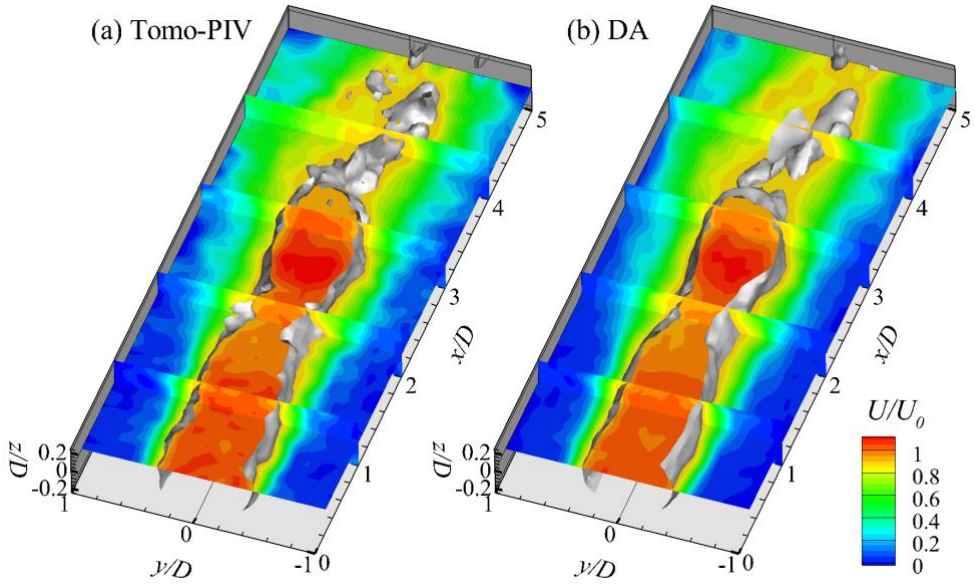

Figure 17 Instantaneous streamwise velocity distributions on the centre plane. Results are interpolated on the same grid. Isosurfaces of $U/U_0 = 0.9$ are shown.

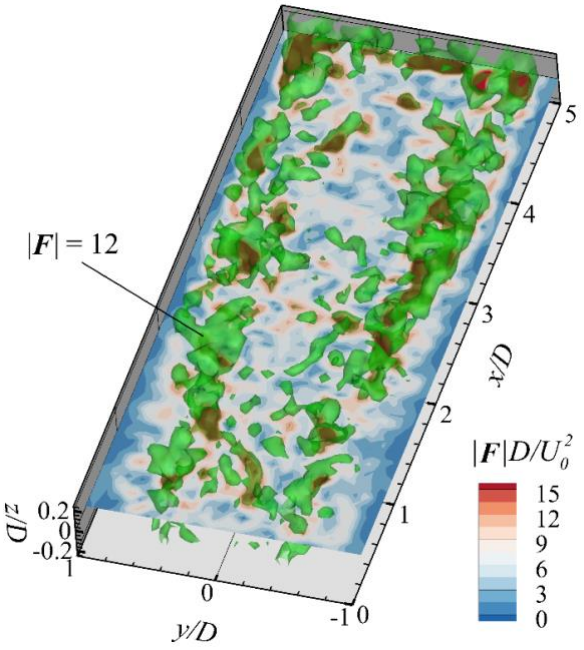

Figure 18 Distribution of the magnitude of the forcing $\boldsymbol{F}$.

The instantaneous pressure fields at three successive instances, determined by the present DA process, are shown in Figure 19 where the organised pressure patterns induced by the vortex rings are clearly seen (black circles). The most significant pattern in the flow field is the fluid puff at $x/D \approx 3$, which results from the fluid acceleration in the centre of the vortex ring, and also yields low-pressure regions both in the ring core (inside the black circles) and advected downstream. Another low-pressure region is also observed at $1 < x/D < 2$ upstream of the pinched-off vortex ring. The pressure in this region keeps decreasing with time, indicating the growth of another vortex ring, before undergoing the pinch-off process. All of these results suggest that the instantaneous pressure fields have been reasonably recovered using the present DA approach.

The pressure field determined by the conventional integration method is also shown in Figure 20. Two adjacent three-dimensional instantaneous velocity fields with a time interval 0.04 s (the time interval of the tomo-PIV measurements) are used for the calculation. Note that high-level measurement noise is contained in the tomo-PIV results, deteriorating both the spatial and temporal coherence. This results in a substantial over-prediction of the pressure magnitude, even when the spatial-temporal smoothing process is used. In fact, the results are sensitive to the noise levels, as the gradients must be calculated in this determination process, and the smoothing does not have much help, except inducing the correlation which is not strictly correct. This pressure pattern is totally different from that in Figure 19, and this method fails to capture the low-pressure regions induced by the vortex rings.

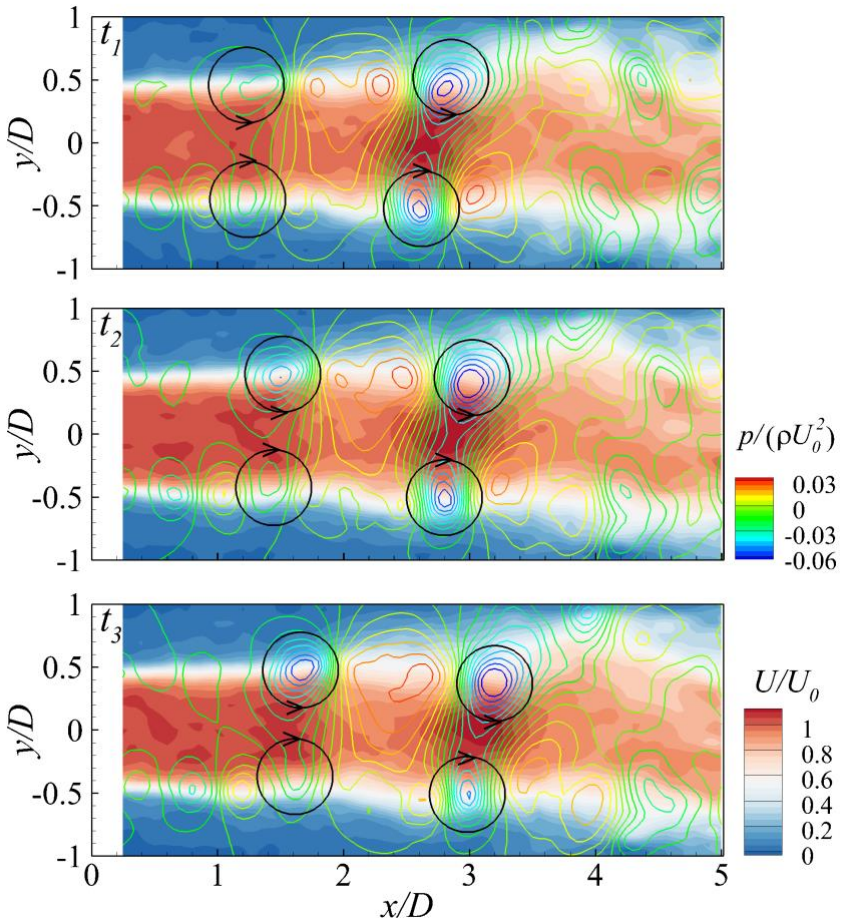

Figure 19 Instantaneous flow (contour) and pressure (isolines) fields determined by the present DA approach. Three successive instances with time interval 0.2 s are shown.

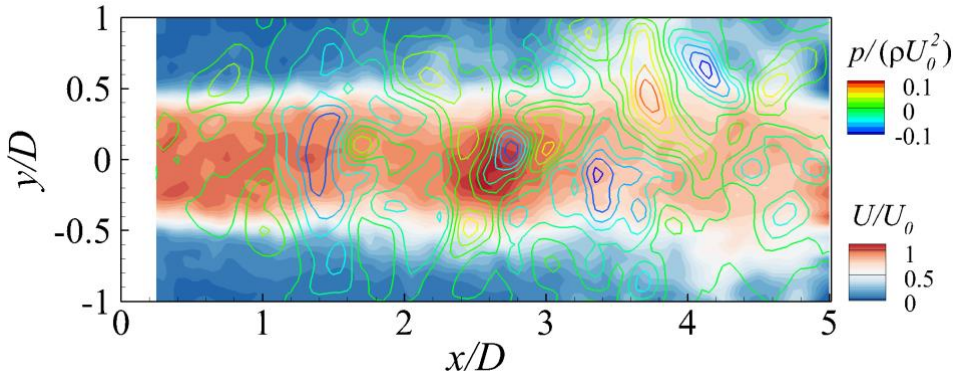

Figure 20 Instantaneous pressure field (isolines) determined by the conventional integration with spatial-temporal smoothing. Velocity field (contour) measured by tomo-PIV at the same instance is also shown.

4. Concluding Remarks

An adjoint-based sequential data assimilation (DA) method was proposed to determine the instantaneous pressure distributions from turbulent velocity fields. The pressure determination method of integration from eight paths[32], modified by considering the off-plane derivatives for three-dimensional flows, was also used for comparison. The DNS data of a laminar cylinder wake, the fine-scale LES data of a turbulent circular jet and the tomo-PIV measurements of a jet flow were used as the observational data to test the properties of this DA method.

In the present DA formulation, a forcing term $\boldsymbol{F}$ was added to the primary Navier-Stokes (N-S) equations to drive the assimilated flow toward the observations at each time step. Compared with the conventional unsteady adjoint method, which required the forward integration of the primary system and the backward integration of the adjoint system, the present approach converted the unsteady adjoint equations to steady versions, by performing the optimisation process at each time-step interval separately. Thus, the computation integrated the primary-adjoint system all the way forward, discarding the requirement of data storage for every time step and also being less demanding on computational resources and space. The adjoint system was solved once the observations were present; otherwise, only the primary equations were solved with $\boldsymbol{F} = 0$, being identical to a pure numerical simulation.

The eight-path integration method was shown to be sensitive to the pressure boundary condition and observational noise contamination, and was subject to the effects of large accumulated error through each path. Using the synthetic data of the turbulent jet as the observational data, the present DA method was able to determine the instantaneous pressure field precisely using the three-dimensional velocity fields, regardless of the observational noise. For the two-dimensional 3C or 2C velocity fields, which were not sufficient for pressure determination with the integration method due to the lack of the off-plane derivatives, the present DA method was able to reproduce pressure fields whose mean and fluctuating fields of both velocity and pressure agreed reasonably well with

those of the reference LES results. The 3C and 2C velocity fields yielded quite similar results, indicating the possibility of pressure determination from planar-PIV measurements in turbulent flows. Tomo-PIV measurements were also tested as the observational data, with a clear pressure pattern induced by the vortex ring obtained with the present DA method, while the eight-path integration method failed to determine the pressure pattern induced by the vortex ring due to the high-level measurement noise.

Acknowledgements

The authors gratefully acknowledge financial support for this study from the National Natural Science Foundation of China (11725209) and the Engineering and Physical Sciences Research Council of the UK (EP/P004377/1).

References

1. W. K. Blake, *Mechanics of flow-induced sound and vibration, Volume 2: Complex flow-structure interactions* (Academic Press, 2017).

2. E. Manoha, B. Troff, and P. Sagaut, "Trailing-edge noise prediction using large-eddy simulation and acoustic analogy," AIAA Journal **38**, 575 (2000).

3. A. Eltaweel, M. Wang, D. Kim, F. O. Thomas, and A. V. Kozlov, "Numerical investigation of tandem-cylinder noise reduction using plasma-based flow control," Journal of Fluid Mechanics **756**, 422 (2014).

4. C. Atkinson, S. Coudert, J.-M. Foucaut, M. Stanislas, and J. Soria, "The accuracy of tomographic particle image velocimetry for measurements of a turbulent boundary layer," Experiments in Fluids **50**, 1031 (2011).

5. G. E. Elsinga, F. Scarano, B. Wieneke, and B. W. van Oudheusden, "Tomographic particle image velocimetry," Experiments in Fluids **41**, 933 (2006).

6. B. Van Oudheusden, "PIV-based pressure measurement," Measurement Science and Technology **24**, 032001 (2013).

7. D. Violato, P. Moore, and F. Scarano, "Lagrangian and Eulerian pressure field evaluation of rod-airfoil flow from time-resolved tomographic PIV," Experiments in Fluids **50**, 1057 (2011).

8. R. de Kat, and B. Ganapathisubramani, "Pressure from particle image velocimetry for convective flows: a Taylor's hypothesis approach," Measurement Science and Technology **24**, 024002 (2012).

9. R. Panciroli, and M. Porfiri, "Evaluation of the pressure field on a rigid body entering a quiescent fluid through particle image velocimetry," Experiments in Fluids **54**, 1630 (2013).

10. S. Pröbsting, F. Scarano, M. Bernardini, and S. Pirozzoli, "On the estimation of wall pressure coherence using time-resolved tomographic PIV," Experiments in Fluids **54**, 1567 (2013).

11. J. J. Charonko, C. V. King, B. L. Smith, and P. P. Vlachos, "Assessment of pressure field calculations from particle image velocimetry measurements," Measurement Science and Technology **21**, 105401 (2010).

12. H.-P. Wang, Q. Gao, S.-Z. Wang, Y.-H. Li, Z.-Y. Wang, and J.-J. Wang, "Error reduction for time-resolved PIV data based on Navier–Stokes equations," Experiments in Fluids **59**, 149 (2018).

13. Z. Pan, "Error Propagation Dynamics of PIV-based Pressure Field Calculation," Brigham Young University, 2016.

14. X. Liu, and J. Katz, "Instantaneous pressure and material acceleration measurements using a four-exposure PIV system," Experiments in Fluids **41**, 227 (2006).

15. J. O. Dabiri, S. Bose, B. J. Gemmell, S. P. Colin, and J. H. Costello, "An algorithm to estimate unsteady and quasi-steady pressure fields from velocity field measurements," Journal of Experimental Biology **217**, 331 (2014).

16. R. de Kat, and B. van Oudheusden, "Instantaneous planar pressure determination from PIV in turbulent flow," Experiments in Fluids **52**, 1089 (2012).

17. J. van der Kindere, A. Laskari, B. Ganapathisubramani, and R. de Kat, "Pressure from 2D snapshot PIV," Experiments in Fluids **60**, 32 (2019).

18. R. de Kat, and B. W. van Oudheusden, *Instantaneous planar pressure from PIV: analytic and experimental test-cases* (Lisbon, Portugal, 2010).

19. N. Fujisawa, S. Tanahashi, and K. Srinivas, "Evaluation of pressure field and fluid forces on a circular cylinder with and without rotational oscillation using velocity data from PIV measurement," Measurement Science and Technology **16**, 989 (2005).

20. R. de Kat, B. W. van Oudheusden, and F. Scarano, *Instantaneous planar pressure field determination around a*

square-section cylinder based on time resolved stereo-PIV (Calouste Gulbenkian Foundation, 2008).
21. S. Ghaemi, D. Ragni, and F. Scarano, "PIV-based pressure fluctuations in the turbulent boundary layer," Experiments in Fluids **53**, 1823 (2012).
22. I. M. Navon, *Data assimilation for numerical weather prediction: a review* (Springer, 2009).
23. A. Mishra, and G. Iaccarino, "Theoretical analysis of tensor perturbations for uncertainty quantification of Reynolds averaged and subgrid scale closures," Physics of Fluids **31**, 075101 (2019).
24. L. Zhu, W. Zhang, J. Kou, and Y. Liu, "Machine learning methods for turbulence modeling in subsonic flows around airfoils," Physics of Fluids **31**, 015105 (2019).
25. A. P. Singh, and K. Duraisamy, "Using field inversion to quantify functional errors in turbulence closures," Physics of Fluids **28**, 045110 (2016).
26. C. He, Y. Liu, and L. Gan, "A data assimilation model for turbulent flows using continuous adjoint formulation," Physics of Fluids **30**, 105108 (2018).
27. C. He, Y. Liu, L. Gan, and L. Lesshafft, "Data assimilation and resolvent analysis of turbulent flow behind a wall-proximity rib," Physics of Fluids **31**, 025118 (2019).
28. M. Lemke, and J. Sesterhenn, "Adjoint-based pressure determination from PIV data in compressible flows—validation and assessment based on synthetic data," European Journal of Mechanics-B/Fluids **58**, 29 (2016).
29. M. Lemke, "Adjoint based data assimilation in compressible flows with application to pressure determination from PIV data," Technische Universität Berlin, 2015.
30. V. Mons, J.-C. Chassaing, and P. Sagaut, "Optimal sensor placement for variational data assimilation of unsteady flows past a rotationally oscillating cylinder," Journal of Fluid Mechanics **823**, 230 (2017).
31. C. He, Y. Liu, and S. Yavuzkurt, "Large-eddy simulation of circular jet mixing: lip-and inner-ribbed nozzles," Computers & Fluids **168**, 245 (2018).
32. L. Armijo, "Minimization of functions having Lipschitz continuous first partial derivatives," Pacific Journal of Mathematics **16**, 1 (1966).
33. N. Worth, and T. Nickels, "Time-resolved volumetric measurement of fine-scale coherent structures in turbulence," Physical Review E **84**, 025301 (2011).
34. L. Gan, J. Cardesa-Duenas, D. Michaelis, and J. Dawson, *Comparison of Tomographic PIV algorithms on resolving coherent structures in locally isotropic turbulence* (Lisbon, Portugal, 2012).